Chemical Science

ROYAL SOCIETY OF CHEMISTRY

EDGE ARTICLE

View Article Online
View Journal | View Issue

Cite this: *Chem. Sci.*, 2025, **16**, 16712

All publication charges for this article have been paid for by the Royal Society of Chemistry

Designing mesostructured bimetallic selenide derived from room-temperature prepared metal–organic frameworks as a sodium-ion battery anode with high performance and fast reaction kinetics

Huizi Songtian,[a] Ting Zhou,[a] Fan Zhou,[b] Yajun Zhu,[ac] Xulai Yang,*[b] Tianli Han,*[a] Jinjin Li *[d] and Jinyun Liu *[a]

Mesostructured materials are considered to be promising candidates for use in high-performance secondary batteries due to their specific properties, which are beneficial for electrochemical redox and ion diffusion; however, the synergistic mechanism is still unclear, and a general preparation approach is highly needed. Here, we report a mesostructured nitrogen-doped $CoNiSe_2$ as a high-performance sodium-ion battery anode derived from room-temperature-synthesized CoNi-metal organic frameworks, and in-depth insight into the synergistic effect during charge–discharge is demonstrated. The mesostructure provides three-dimensional ion transport channels, which are conducive to the stable insertion/extraction of Na^+ ions. *In situ* Raman spectra and *in situ* X-ray diffraction patterns verify the good real-time reversibility of the mesostructured $CoNiSe_2$/NC upon charge–discharge. Moreover, $CoNiSe_2$/NC shows fast reaction kinetics and enhanced electrical conductivity. The results show that the $CoNiSe_2$/NC anode displays a high and stable capacity of 498 mAh g^{-1} after 600 cycles at 0.2 A g^{-1}, and 426 mAh g^{-1} after being cycled 1500 times at 1 A g^{-1}, exceeding the performance of many reported anodes. Even at 50 °C or −10 °C, the anode exhibits stable performance. In addition, the full cell provides 270 mAh g^{-1} after 500 cycles at 0.5 A g^{-1}, exhibiting promising potential for practical applications. These findings are important for developing emerging energy-storage materials and will find broad applications in many battery systems.

Received 1st May 2025
Accepted 5th August 2025

DOI: 10.1039/d5sc03181h

rsc.li/chemical-science

Introduction

In recent years, the demand for energy has been increasing, and rechargeable batteries have become an indispensable part of energy-storage systems. Lithium-ion (Li-ion) batteries are widely used; however, due to the continuous increase in market demand, the shortage of lithium resources has become a widespread concern.[1] Sodium (Na) is more abundant in the Earth's crust compared to Li, while Na and Li have similar chemical properties, making Na-ion batteries a promising alternative to Li-ion batteries.[2] Nevertheless, the larger radius of Na^+ ions compared to Li^+ leads to poor cycling stability and slow kinetic reactions. Among the many challenges, the development of ideal anode materials with high capacity and fast reaction kinetics is of great significance.

Metal sulfides commonly have high theoretical capacity, low cost and higher conductivity compared to metal oxides. However, structural collapse due to the volume change of metal sulfides during cycling accelerates the consumption of Na^+ ions and causes irreversible side reactions, resulting in rapid capacity loss.[3] Selenium (Se) and sulfur (S) belong to the same main group. Compared to some transition metal sulfides, selenides have higher electrical conductivity and better absorption coefficients, which enable them to have good electrochemical performances in secondary battery systems.[4]

To date, many metal selenides have been prepared for Na-ion batteries. For example, Kang *et al.* synthesized $CoSe_2$/N using a hydrothermal method, which exhibited 450.1 mAh g^{-1} after 100 cycles at 0.2 A g^{-1}.[5] However, compared to single-metal selenides, bimetallic and multi-metal selenides can provide more reaction sites, and thus improve energy-storage performance.[6] Li *et al.* prepared CoSe/$MoSe_2$–C microspheres through a hydrothermal method, which exhibited a capacity of 320.9 mAh g^{-1} at 2 A g^{-1}.[7] Zhang *et al.* synthesized $FeSe_2$@$CoSe_2$/

[a]*Key Laboratory of Functional Molecular Solids, Ministry of Education, College of Chemistry and Materials Science, Anhui Normal University, Wuhu, Anhui 241002, PR China. E-mail: hantianli@ahnu.edu.cn; jyliu@iim.ac.cn*

[b]*School of Advanced Manufacturing Engineering, Hefei University, Hefei, Anhui 230069, PR China. E-mail: yangxl@hfuu.edu.cn*

[c]*Institute of Energy, Hefei Comprehensive National Science Center, Hefei, Anhui 230031, PR China*

[d]*National Key Laboratory of Science and Technology on Micro/Nano Fabrication, Department of Micro/Nano-electronics, Shanghai Jiao Tong University, Shanghai 200240, PR China. E-mail: lijinjin@sjtu.edu.cn*

$FeSe_2$ nanofibers using an electrospinning technology, which displayed good electrochemical performances.[8] Zhou *et al.* synthesized CoNi-BTC using a hydrothermal method at 160 °C for 12 hours, and then further obtained $CoNiSe_2$/C *via* high-temperature selenization.[9] In addition, it was reported that the structural integrity of selenides can be enhanced by encapsulation in carbon.[10] This is attributed to the fact that the highly conductive carbon can protect the selenide core and accelerate electron transport upon charging and discharging, thereby improving the electrochemical performance.[11] Currently, most reports on the synthesis of metal selenides focus on the use of the hydrothermal method at relatively high temperature, which requires high costs and long reaction times, and makes it difficult to control the morphology. Thus, the development of a low-energy-consumption and general method to prepare selenides with controllable structure is needed. In addition, hierarchical dimensions such as micro- and nano-structures in mesostructures can endow them with specific properties for fast electron and ion transfer, and high exposure of active sites in chemical reactions.[12,13] These advantages make mesostructures promising for secondary battery systems; however, simple and general preparation strategies are still urgently required, and in-depth investigations into real-time charging and discharging remain a great challenge.

Here, we report a mesostructured nitrogen-doped $CoNiSe_2$ ($CoNiSe_2$/NC) prepared through a universal synthesis method by using room-temperature synthesized metal organic frameworks (MOFs) as precursor. The mesostructured $CoNiSe_2$/NC has a hollow and porous cubic morphology assembled by numerous nanoparticles, which could provide short paths for Na^+ ion diffusion and improve penetration of the electrolyte, and the bimetallic phase facilitates rapid electrochemical kinetics. The CoNiSe/NC anode exhibits a high specific capacity of 426 mAh g^{-1} after being cycled 1500 times at 1 A g^{-1}, and it can still be stably cycled at 50 °C and −10 °C. A full cell constructed of a $CoNiSe_2$/NC anode and $Na_3V_2(PO_4)_3$ (NVP) cathode also shows high and stable capacities, demonstrating good potential for broad applications.

Results and discussion

Fig. 1a shows the preparation process of the mesostructured $CoNiSe_2$/NC using a room-temperature-prepared CoNi-MOF precursor. In Fig. 1b and S1 (SI), transmission electron microscope (TEM) images of the CoNi-MOF precursor are presented, which exhibits a nanocubic structure with a size of about 200 nm. Fig. S2 shows the XRD pattern of the CoNi-MOF precursor, which is indexed to a topological ZIF-67 structure with Ni^{2+} introduced in the system.[14,15] Scanning electron microscopy (SEM) and TEM photographs (Fig. 1c and d) demonstrate a porous and hollow morphology composed of nanoparticles. Fig. 1e presents a high-resolution TEM (HRTEM) image of $CoNiSe_2$/NC with lattice spacings of 0.203 and 0.298 nm corresponding to the (102) and (100) planes of $CoNiSe_2$/NC. In addition, the selected area electron diffraction (SAED) pattern (Fig. 1f) confirms a polycrystalline structure. Fig. 1g shows the Rietveld refinement X-ray diffraction (XRD)

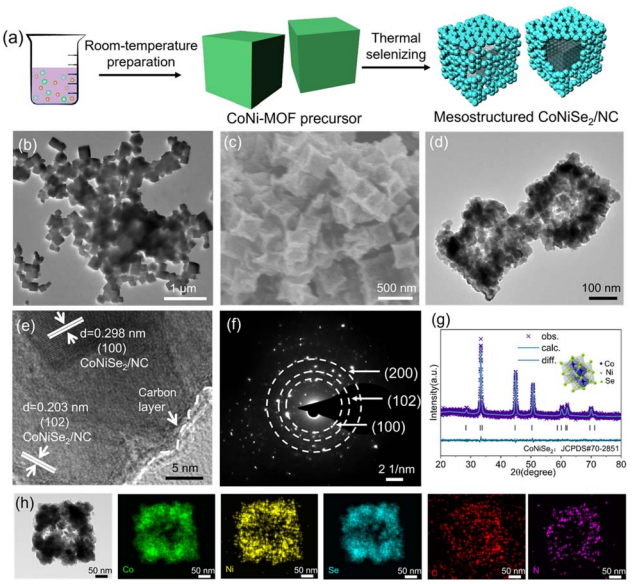

Fig. 1 (a) Illustration of the preparation of mesostructured $CoNiSe_2$/NC. (b) TEM image of the CoNi-MOF precursor. (c) SEM, (d) TEM, and (e) HRTEM images, (f) SAED pattern, and (g) XRD Rietveld refinement results of $CoNiSe_2$/NC. (h) TEM and mapping images.

pattern of $CoNiSe_2$/NC, which indicates a cubic space group of $P\bar{3}m1$ with lattice parameters of $a = b = 3.65$ Å and $c = 5.17$ Å. Furthermore, the XRD patterns of $CoNiSe_2$/NC, CoSe/NC, and NiSe/NC are displayed in Fig. S3 (SI). Since Co and Ni are transition metal elements from the same period, the nature of their chemical bonds with Se is similar, leading to similar diffraction peaks. However, the difference in atomic radius between Co and Ni causes the peaks of CoSe to shift to the right compared to those of $CoNiSe_2$, while those of NiSe shift toward the left. The elemental mappings in Fig. 1h demonstrate a uniform distribution of Co, Ni, Se, N, and C. For comparison, we synthesized Co-MOFs and Ni-MOFs through the same method at room temperature and further selenized them to form CoSe/NC and NiSe/NC. SEM images of the Co-MOFs, Ni-MOFs, CoSe/NC and NiSe/NC are shown in Fig. S4 (SI). The Co-MOFs show a cubic morphology, while the Ni-MOFs exhibit a layered morphology which may be caused by the lack of structural support of Co atoms. The energy-dispersive spectroscopy (EDS) spectrum of $CoNiSe_2$/NC is displayed in Fig. S5 (SI), and indicates that the $CoNiSe_2$/NC has a high purity.

The specific surface area and pore size of $CoNiSe_2$/NC in Fig. S6 and S7 (SI) show a typical mesoporous structure with a specific surface area of 88.67 m^2 g^{-1} and a dominating pore size of 11.23 nm. An appropriate pore size can facilitate electrolyte penetration, thus improving the electrochemical properties. The chemical states of $CoNiSe_2$/NC were analyzed using X-ray photoelectron spectroscopy (XPS), as displayed in Fig. S8 (SI). In the full spectrum, Co, Ni, Se, N, and C are clearly observed. The presence of the element O could be ascribed to the absorption of oxygen from the air.[16] In the Co 2p spectrum, the peaks at 780.6 and 796.7 eV correspond to Co^{2+} with Co $2p_{3/2}$ and Co $2p_{1/2}$; those at 777.8 and 793 eV are assigned to Co^{3+} with

Co $2p_{3/2}$ and Co $2p_{1/2}$, respectively. The peaks at 785.5 and 802.5 eV are indexed to satellite peaks.[17] For the Ni 2p spectrum, the peaks at 852.7 and 855.2 eV as well as that at 872.7 eV are assigned to Ni^{2+} with Ni $2p_{3/2}$ and Ni $2p_{1/2}$, while the weak ones at 860.38 and 879.8 eV are satellite peaks.[18] In the Se 3d spectrum, the peaks at 53.7, 54.4, and 59.2 eV are indexed to Se $3d_{5/2}$, Se $3d_{3/2}$, and SeO_x, respectively.[19] The C 1s spectrum shows three peaks corresponding to C=C/C–C (284.8 eV), C–N (285.3 eV), π–π* (295 eV).[20,21,28] According to some reports,[22,23] high-temperature carbonization is usually accompanied by carbon graphitization, which will enhance the continuity of the sp^2-hybridized carbon, thereby facilitating the formation of π–π*. This is verified by the Raman spectra (Fig. S9, SI), in which the $CoNiSe_2$/NC shows D and G bands at 1345 and 1594 cm^{-1} with an I_D/I_G ratio of 0.8, indicating that the graphitization degree of carbon is relatively high. Additionally, the doping with N would influence the electronic distribution of the carbon, enhancing the delocalization of the π electrons and promoting the formation of π–π*. The peaks in the N 1s spectrum correspond to pyridinic N (398.1 eV), pyrrolic N (400 eV), graphitic N (401.7 eV), and oxidized N (405.9 eV), verifying efficiently N-doped carbon.[24] Thermogravimetric analysis (TGA, Fig. S10, SI) of $CoNiSe_2$/NC displays a weight loss starting at 250 °C, which is caused by the volatilization of adsorbed water. The increase of weight in the range of 250–400 °C is attributed to the oxidation of $CoNiSe_2$. The subsequent straight drop from 400 °C to 650 °C is ascribed to both volatilization of CO_2 and sublimation of SeO_2, since $CoNiSe_2$ is oxidized to NiO, Co_3O_4 and SeO_2 following the equation $6CoNiSe_2 + 19O_2 = 6NiO + 2Co_3O_4 + 12SeO_2\uparrow$, and carbon is converted to CO_2.[9,25,26] On the basis of the TGA results, it is calculated that the carbon content in $CoNiSe_2$/NC is about 5.59 wt%.

Fig. 2a shows galvanostatic charging–discharging (GCD) profiles of $CoNiSe_2$/NC at 0.2 A g^{-1}. The initial coulombic efficiency (ICE) is 73.4%, which is attributed to SEI formation; however, the CE increases to about 100% in subsequent cycles. In Fig. 2b, a reduction peak is observed at 0.9 V during the initial cathodic scanning, which is different from the peak position in subsequent charge and discharge. This is ascribed to irreversible interfacial reactions during the first cathodic process, resulting in the reaction of $CoNiSe_2$ with Na^+ ions to form the intermediate $Na_xCoNiSe_2$.[27,28] Due to the continuous insertion of Na^+ ions, the intermediate phase eventually converts to Co, Ni, CoNiSe, and Na_2Se.[29] In the charging process, the oxidation at 1.76 V corresponds to the conversion of Co, Ni, and Na_2Se. After the first cycle, the reduction peak shifts to 1.3 V. In the subsequent cycles, the redox peak positions almost overlap, indicating that the $CoNiSe_2$/NC has good reversibility. It is noted that the discharge plateau in the first cycle appears at around 0.9 V, while in the second cycle it presents at 1.3 V. This is consistent with the CV curves, indicating the formation of intermediate phases.

For comparison, CV measurements were also conducted on CoSe/NC and NiSe/NC anodes (Fig. S11, SI). The peak positions are similar. However, the polarization of $CoNiSe_2$/NC is small, suggesting that the electrochemical reaction resistance of $CoNiSe_2$/NC is low and the reaction kinetics is fast. Fig. 2c

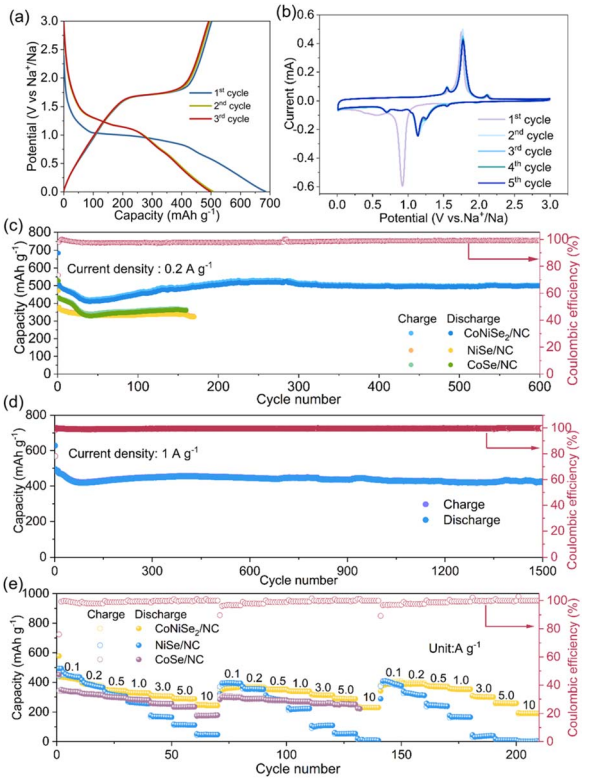

Fig. 2 (a) GCD curves of the $CoNiSe_2$/NC anode at 0.2 A g^{-1}. (b) CV profiles of the $CoNiSe_2$/NC anode at 0.1 mV s^{-1}. Electrochemical performances at (c) 0.2 and (d) 1.0 A g^{-1}. (e) Rate-performances. All CEs are from the $CoNiSe_2$/NC anode.

shows that $CoNiSe_2$/NC exhibits a high capacity of 498 mAh g^{-1} after 600 cycles at 0.2 A g^{-1}, while CoSe/NC and NiSe/NC show 360 and 323 mAh g^{-1}, respectively. Fig. 2d displays the cycling of $CoNiSe_2$/NC at 1.0 A g^{-1}. After 1500 cycles, the capacity exceeds 426 mAh g^{-1}, exhibiting an excellent cycling stability. Compared with some other types of materials such as microporous $Co_{0.85}Se$@carbon nanotubes growing on carbon microplates ($Co_{0.85}Se$@CNT–CP) and macro-porous $Ni_{0.85}Se$@C,[30–32] the mesostructured $CoNiSe_2$/NC presented here shows competitive performances. This is attributed to the mesostructured structure that provides appropriate and rapid transport channels for Na^+ ions, shortening the diffusion distance. Additionally, the mesoporous morphology enables a larger specific surface area, which offers numerous active sites, allowing the electrolyte to fully contact the electrode. This is conducive to the insertion/extraction of Na^+ ions, thereby improving the charging and discharging efficiency and capacity. The hollow morphology also effectively alleviates the volume-change. The structure of $CoNiSe_2$/NC after cycling at 0.5 A g^{-1} was characterized (Fig. S12, SI). The morphology is well maintained without collapse, indicating that the structure is robust. Moreover, we synthesized CoNi-MOFs using a hydrothermal method at 160 °C for 12 h, and then carried out thermal selenization to obtain $CoNiSe_2$/NC. As shown in Fig. S13 (SI), the $CoNiSe_2$/NC exhibits a capacity of 395 mAh g^{-1} after 50 cycles at 1 A g^{-1}. This is slightly lower than that of the $CoNiSe_2$/NC

prepared using the room-temperature synthesized precursor, which indicates that the room-temperature-based approach not only reduces the preparation cost, but also achieves competitive performances. In addition, the cycling performance was compared with that of some other anodes (Table S1, SI), which indicated that the mesostructured $CoNiSe_2$/NC has a good performance.

The rate-performance at current densities from 0.1 to 10 A g^{-1} is displayed in Fig. 2e. Even in the third round, when the current density is reverted to 0.1 A g^{-1}, $CoNiSe_2$/NC recovers to 406 mAh g^{-1} with a retention rate of 95.3%, further conforming a highly reversible performance. In contrast, CoSe/NC displays 305 mAh g^{-1} with a retention rate of 90.1%, and NiSe/NC exhibits 386 mAh g^{-1} and a retention rate of 86.9%. This is ascribed to the mesostructured bimetallic selenide being able to provide active sites for electrochemical reactions under different charging/discharging speeds.[33,34]

In order to study the kinetics of the $CoNiSe_2$/NC anode, we further conducted CV scans in the range of 0.1–1.0 mV s^{-1} (Fig. S14, SI). The CV strength of $CoNiSe_2$/NC is shown in Fig. 3a, which indicates that the charge response is fast, which is achieved by the improved conductivity with the carbon coating. In order to explore the kinetic characteristics of the electrode reaction, the formulas $i = av^b$, where i is peak current; v is scanning rate; a and b are adjustable parameters, and $\log(i) = b\log(v) + \log(a)$ were employed. The slope obtained by linear fitting of the peak current and scanning rate through $\log(i) = b\log(v) + \log(a)$ indicates the b value. In Fig. 3b, the b values of $CoNiSe_2$/NC are 0.68, 0.70, 0.92, 0.93, indicating that the anode reaction is controlled by diffusion and pseudocapacitance.[35]

The CV curves of NiSe/NC and CoSe/NC are shown in Fig. S15 (SI); while the b values are presented in Fig. S16 (SI). According to $i = k_1v + k_2v^{1/2}$, $i/v^{1/2} = k_1v^{1/2} + k_2$, the contribution rate of pseudocapacitance was studied, and the contribution rate is shown in Fig. 3c. With the increase of scanning speed, the contribution rate of pseudocapacitance increases from 78.06% to 92.58%. Compared with those of NiSe/NC and CoSe/NC, the reaction kinetics of $CoNiSe_2$/NC is significantly faster, indicating that the bimetallic mesostructure improves the redox kinetics.

As shown in Fig. S17 (SI), the decay of IR and dE_τ of $CoNiSe_2$/NC is smaller than that of NiSe/NC and CoSe/NC (Fig. S18, SI). The *in situ* internal resistance was analyzed using the galvanostatic intermittent titration technique (GITT, Fig. S19, SI). Fig. 3d and e show that the internal resistance of $CoNiSe_2$/NC is lower than those of NiSe/NC and CoSe/NC, indicating that $CoNiSe_2$/NC has a lower barrier and better electrical conductivity. The discharging resistances at 1.8 to 0.2 V and the charging ones at 0.4 to 3.0 V are shown in Fig. 3f and g. Distribution of relaxation times (DRT) analysis was employed to show the change in the resistance directly. Fig. 3h shows that the charge transfer resistance (R_{ct}) of $CoNiSe_2$/NC decreases rapidly when being discharged from 1.8 to 0.2 V, which is caused by the formation of transition metals, facilitating electron transfer. During the charging process (Fig. 3i), the R_{ct} value of $CoNiSe_2$/NC increases slowly, then tends to be stable. The R_{SEI} remains stable during charge, which indicates good interface stability.[36]

The real-time Na storage process was analyzed using *in situ* Raman spectroscopy (Fig. 4a). During the discharge, E_g and

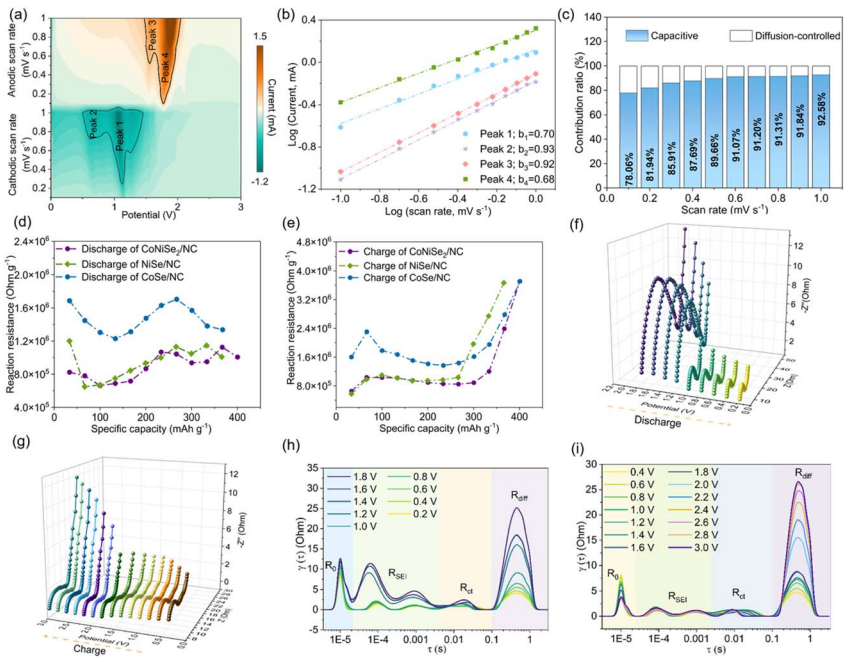

Fig. 3 (a) CV strength map of $CoNiSe_2$/NC. (b) $\log(i)$ *vs.* $\log(v)$ of the oxidization and reduction peaks of $CoNiSe_2$/NC, and (c) ratio of pseudocapacitive contribution. Reaction resistances of $CoNiSe_2$/NC during (d) discharge and (e) charge. Nyquist plots of $CoNiSe_2$/NC at (f) discharge and (g) charge during the initial cycle. Distribution of relaxation times (DRT) contour pattern corresponding to the EIS spectra from (h) 1.8 to 0.2 V and (i) 0.4 to 3.0 V for the first cycle.

F^1_{2g} peaks at 457 and 540 cm^{-1} corresponding to the stretching vibrations of Co–Se and Ni–Se bonds are observed. The A^1_g peak at 786 cm^{-1} is indexed to symmetrical stretching vibrations of the Co–Se and Ni–Se bonds,[37] and gradually disappears during discharge. This indicates that the Co–Se and Ni–Se bonds break and then generate Na_2Se depending on the intercalation of Na^+ ions. During the charging process to 2.6 V, the E_g, F^1_{2g} and A^1_g peaks are again detected, indicating that the insertion/extraction of Na^+ ions has good reversibility. In Fig. 4b, the D and G bands of carbon are observed. When the potential is decreased from 1.8 to 0.1 V, the D band broadens significantly, while the peak position remains stable, which is attributed to the adsorption of Na^+ ions at the defects and pores, thereby limiting the stretching vibration of the sp^2 carbon ring at defects and edges.[38,39] During this period, a slight redshift of the G band occurs, which would be attributed to the transfer of electrons from cations to the graphite layer during the intercalation of Na^+ ions, filling the π^* anti-bond orbitals and thereby weakening the C–C bond.[40,41] After charging, the D and G bands return to the initial state reversibly. In order to further investigate the phase-change reversibility of the $CoNiSe_2$/C anode, *in situ* XRD patterns (Fig. 4c) were measured. At the beginning of discharge, peaks of $CoNiSe_2$ (JCPDS: 70-2581) at 33.7°, 45.5°, 60.9°, and 62.8° are observed. As the Na^+ ions are intercalated, the signals of the $CoNiSe_2$ peaks gradually weaken until they disappear completely. A new peak appears at 38.4°, which corresponds to the (220) plane of Na_2Se (JCPDS: 77-2155). The peak at 45.6° corresponds to the (111) plane of metallic Ni (JCPDS: 88-2326) and Co (JCPDS: 88-2325). After fully discharging, $CoNiSe_2$ is transformed into Na_2Se. In the subsequent charging process, as the peak of Na_2Se gradually diminishes, the peaks of $CoNiSe_2$ appear again, which further verifies the good reversible transformation of $CoNiSe_2$ during charge and discharge.

In addition, the electrochemical impedance spectroscopy (EIS) spectra of $CoNiSe_2$/NC, NiSe/NC and CoSe/NC are shown in Fig. S20 (SI). The fitting results indicate that the R_{ct} of $CoNiSe_2$/NC, NiSe/NC and CoSe/NC are 21.68, 36.22 and 57.71 Ω, respectively. The internal resistances of $CoNiSe_2$/NC, NiSe/NC and CoSe/NC cycled at 0.5 A g^{-1} after 100 cycles are 6.72, 9.25 and 17.4 Ω, respectively. The significant decrease in the R_{ct} of $CoNiSe_2$/NC is ascribed to the enhanced electronic conductivity.

The cycling performance of $CoNiSe_2$/NC at a high temperature is shown in Fig. 5a. At 50 °C, the capacity is maintained at 433 mAh g^{-1} after 700 cycles at 1.0 A g^{-1}, which indicates that

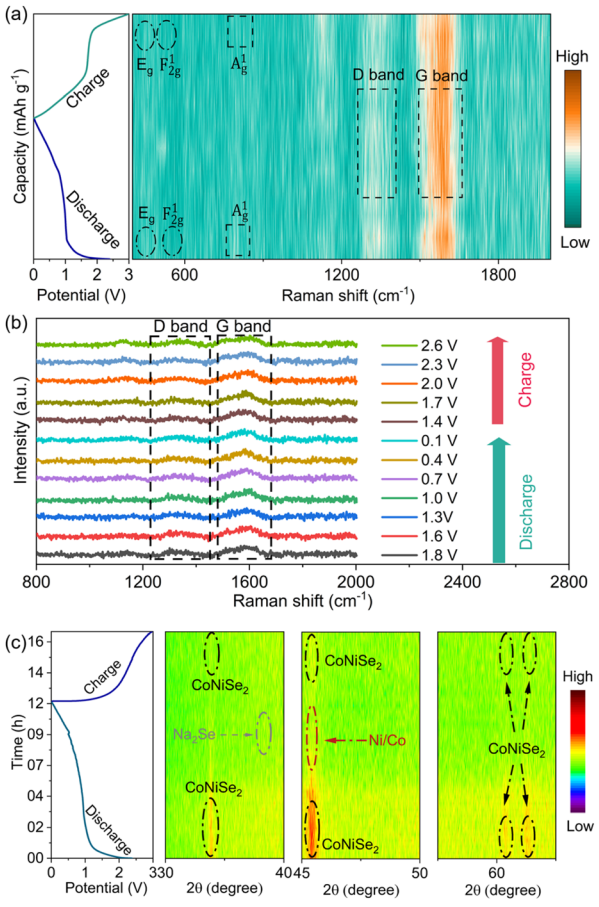

Fig. 4 (a) Contour plots of *in situ* Raman spectra of $CoNiSe_2$/NC anode during the charging–discharging process. (b) Raman spectra at a series of potentials. (c) Contour plots of the *in situ* XRD patterns of $CoNiSe_2$/NC upon charge and discharge.

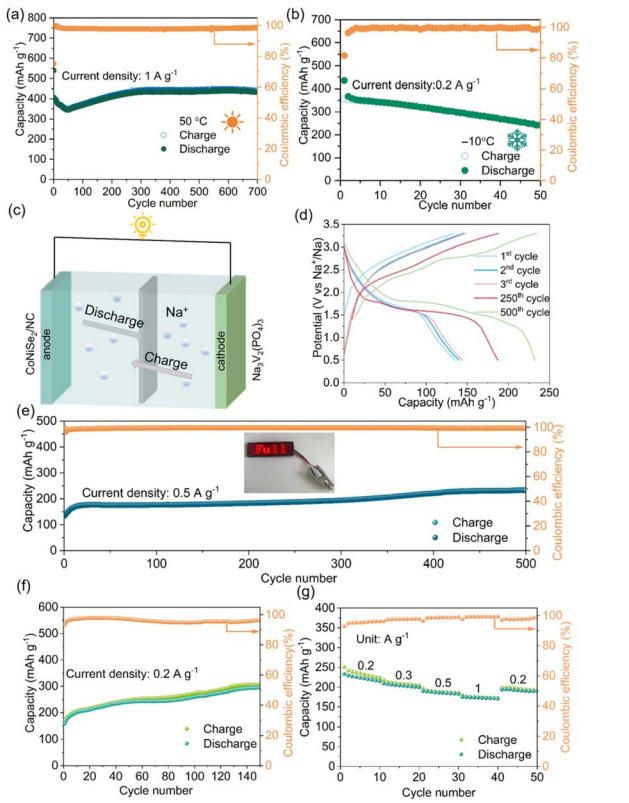

Fig. 5 (a) Cycling performance of the $CoNiSe_2$/NC anode at 1.0 A g^{-1} under 50 °C. (b) Cycling performance of the $CoNiSe_2$/NC anode at 0.2 A g^{-1} under −10 °C. (c) Schematic of a $CoNiSe_2$/NC||NVP full cell. (d) GCD curves of the full cell at 0.5 A g^{-1}. Electrochemical performances at (e) 0.5 and (f) 0.2 A g^{-1}. The insert in (e) shows LEDs lighted by a full cell. (g) Rate-performance of the full cell after pre-activation at 0.1 A g^{-1} for 10 cycles. All CEs are from the $CoNiSe_2$/NC anode.

the anode has good thermal stability. Furthermore, the low-temperature performance under −10 °C (Fig. 5b) at 0.2 A g^{-1} demonstrates that the $CoNiSe_2$/NC remains stable after being cycled 50 times, indicating good potential for practical applications. In addition, full cells were fabricated using a $CoNiSe_2$/NC anode and $Na_3V_2(PO_4)_3$ (NVP) cathode. In Fig. S21 (SI), the NVP cathode exhibits stable capacity and rate-performance with stable voltage plateaus. This is conducive to achieving good performance for the full-cell system working with the $CoNiSe_2$/NC anode presented here. The schematic diagram of the full cell is illustrated in Fig. 5c, and GCD curves are presented in Fig. 5d. Stable plateaus are displayed, which indicate complete electrochemical reactions in the full cells. Fig. 5e and f display the cycling performances at 0.5 and 0.2 A g^{-1}. After being cycled 150 times at 0.2 A g^{-1}, the capacity is maintained at 302 mAh g^{-1}, while when cycled at 0.5 A g^{-1}, the capacity is maintained at 230 mAh g^{-1} after 500 cycles. It is noted that the reversibility and CEs at 0.2 A g^{-1} are relatively low, which would be ascribed to the non-ideal mass matching between the anode and cathode, which could be further improved by adjusting the optimal ratio. Fig. 5g shows the rate-performance of the full cell. After cycling at 1 A g^{-1}, once the current density is returned to 0.2 A g^{-1}, the capacity recovers to the initial value, demonstrating reversibility. The initial capacity at 0.2 A g^{-1} during rate-performance tests is relatively higher compared to that in Fig. 5f, which is ascribed to the pre-activation effect. These results indicate good compatibility between the NVP cathode and the presented $CoNiSe_2$/NC anode for possible applications.

Conclusions

In summary, we have developed a mesostructured $CoNiSe_2$/NC derived from room-temperature-prepared MOFs, which exhibits high performance as a Na-ion battery anode material. *In situ* Raman spectra and *in situ* XRD patterns verify the good real-time reversibility of the mesostructured $CoNiSe_2$/NC upon charge–discharge. GITT and CV curves demonstrate that $CoNiSe_2$/NC has fast reaction kinetics, while EIS spectra indicate its enhanced electrical conductivity. The $CoNiSe_2$/NC anode exhibits a high capacity of 498 mAh g^{-1} after 600 cycles at 0.2 A g^{-1} and 426 mAh g^{-1} after 1500 cycles at 1 A g^{-1}. After three rounds of rate-performance measurements, the $CoNiSe_2$/NC anode has a capacity retention rate as high as 95.3%. Even at 50 °C and −10 °C, the anode shows good cycling performance. In addition, the $CoNiSe_2$/NC||NVP full cell shows good and stable capacity after 500 cycles, indicating that the presented $CoNiSe_2$/NC anode has good practical applicability. These findings provide a general strategy for preparing high-performance Na-ion battery anodes, and we believe that the mesostructured design and synergic enhancement mechanism will find broad applications for engineering many other emerging energy-storage composites.

Author contributions

J. Y. L. conceived the project. J. Y. L. and H. Z. S. wrote the manuscript. H. Z. S. performed most of the characterizations and performance tests. T. Z., F. Z., and Y. J. Z. participated in the experiments and analysis. X. L. Y., T. L. H., J. J. L., and J. Y. L. reviewed and revised the manuscript and supervised the investigation.

Conflicts of interest

There are no conflicts to declare.

Data availability

The data supporting this article have been included as part of the SI. See DOI: https://doi.org/10.1039/d5sc03181h.

Acknowledgements

This work was supported by the Major Science and Technology Research Project of Anhui (2023z020003), Major Science and Technology Research Project of Wuhu (2024zd02), and Anhui Quality Engineering Projects (2022xqhz020 and 2023qygzz007), and Natural Science Research Project for Universities in Anhui Province (2022ah050176).

Notes and references

1 J. Z. Wang, J. J. Li, Q. Zhang, W. Du, H. M. Abo-Dief, S. Melhi, R. Sellami, J. Guo, C. X. Hou and X. Q. Sun, *Adv. Compos. Hybrid Mater.*, 2024, **119**, 7.
2 S. C. Dey, B. Worfolk, L. Lower, W. J. Sagues, M. R. Nimlos, S. S. Kelley and S. Park, *ACS Energy Lett.*, 2024, **9**, 2590–2614.
3 H. Zheng, D. K. Ma, M. J. Pei, C. K. Lin, Y. Liu, S. Q. Deng, R. X. Qiu, Y. Y. Luo, W. Yan and J. J. Zhang, *Adv. Funct. Mater.*, 2025, **35**, 2411651.
4 L. Habib, G. Q. Suo, C. J. Lin, J. R. Li, S. Javed, K. Naseem and Z. K. Kalkozova, *Renewable Sustainable Energy Rev.*, 2025, **217**, 115721.
5 J. L. Kang, Y. X. Yuan, W. Lu, Y. L. Chen, L. L. Hu, D. D. Ai, J. T. Wang and X. Y. Hou, *Appl. Surf. Sci.*, 2024, **672**, 160786.
6 D. Y. Qu, Q. Y. Li, Z. H. Sun, C. Y. Wei, Z. Y. Gu, X. X. Zhao, B. L. Zhao, D. X. Han, L. Niu and X. L. Wu, *Adv. Funct. Mater.*, 2024, 2421504.
7 J. H. Li, Y. Y. He, Y. X. Dai, H. Z. Zhang, Y. X. Zhang, S. A. Gu, X. Wang, T. T. Gao, G. W. Zhou and L. Q. Xu, *Adv. Funct. Mater.*, 2024, **34**, 2406915.
8 L. Y. Zhang, B. C. Zhu, D. F. Xu, Z. B. Qian, P. Xie, T. Liu and J. G. Yu, *J. Mater. Sci. Technol.*, 2024, **172**, 185–195.
9 P. Zhou, L. P. Wang, M. Y. Zhang, F. X. Wu, Q. Z. Huang, Z. Su, P. Xu, M. D. Liao, Y. L. Hu and X. B. Lin, *ACS Appl. Energy Mater.*, 2023, **6**, 7129–7137.
10 G. Q. Suo, B. G. Zhao, R. R. Mu, C. J. Lin, S. Javed, X. J. Hou, X. H. Ye, Y. L. Yang and L. Zhang, *J. Energy Storage*, 2024, **77**, 109801.
11 B. G. Zhao, G. Q. Suo, R. R. Mu, C. J. Lin, J. R. Li, X. J. Hou, X. H. Ye, Y. L. Yang and L. Zhang, *J. Colloid Interface Sci.*, 2025, **677**, 637–646.

12 S. Huang, D. J. Yang, X. Q. Qiu, W. L. Zhang, Y. L. Qin, C. W. Wang and C. H. Yi, *Adv. Funct. Mater.*, 2022, **32**, 2203279.
13 L. Peng, H. R. Peng, S. Wang, X. J. Li, J. Y. Mo, X. Wang, Y. Tang, R. C. Che, Z. K. Wang, W. Li and D. Y. Zhao, *Nat. Commun.*, 2023, **14**, 8148.
14 M. U. Tahir, H. Arshad, H. Zhang, Z. Y. Hou, J. D. Wang, C. Yang and X. T. Su, *J. Colloid Interface Sci.*, 2020, **579**, 195–204.
15 Z. Andikaey, A. A. Ensafi, B. Rezaei and J. S. Hu, *Electrochim. Acta*, 2022, **417**, 140338.
16 Q. Xiao, Q. L. Song, K. Zheng, L. Zheng, Y. Y. Zhu and Z. H. Chen, *Nano Energy*, 2022, **98**, 107326.
17 L. Gao, M. L. Cao, C. K. Zhang, J. Li, X. F. Zhu, X. K. Guo and Z. Toktarbay, *Adv. Compos. Hybrid Mater.*, 2024, **7**, 144.
18 B. Yan, H. Sun, X. P. Liu, X. Y. Fu, C. Q. Xu, T. T. Zhang, H. C. Tao, L. L. Zhang, X. F. Li, X. L. Yang and R. H. Wang, *Energy Environ. Sci.*, 2024, **17**, 3419–3432.
19 J. Y. Weng, D. G. Zou, W. Y. Yuan, P. F. Zhou, M. H. Ding, J. Zhou, H. L. Cong and F. Y. Cheng, *J. Energy Chem.*, 2024, **91**, 407–416.
20 Z. K. Jia, Y. S. Ma, L. Y. Yang, C. P. Guo, N. Zhou, M. H. Wang, L. H. He and Z. H. Zhang, *Biosens. Bioelectron.*, 2019, **133**, 55–63.
21 J. R. Geng, Y. H. Huang, Y. H. Guo, H. X. Li and F. J. Li, *Angew. Chem., Int. Ed.*, 2024, **63**, e202405066.
22 A. Q. Zhang, H. Zhang, B. Hu, M. H. Wang, S. Zhang, Q. J. Jia, L. H. He and Z. H. Zhang, *J. Colloid Interface Sci.*, 2022, **608**, 1257–1267.
23 T. S. Wang, H. K. Kim, Y. J. Liu, W. W. Li, J. T. Griffiths, Y. Wu, S. Laha, K. D. Fong, F. Podjaski, C. Yun, R. V. Kumar, B. V. Lotsch, A. K. Cheetham and S. K. Smoukov, *J. Am. Chem. Soc.*, 2018, **140**, 6130–6136.
24 H. Li, Y. Y. He, Q. Wang, S. A. Gu, L. Wang, J. X. Yu, G. W. Zhou and L. Q. Xu, *Adv. Energy Mater.*, 2023, **13**, 2302901.
25 Y. H. Zhang, J. L. Wang, H. Y. Yan, J. T. Zhao, D. D. Wang, S. H. Luo, Q. Wang and X. Liu, *Ionics*, 2023, **29**, 3505–3515.
26 M. Jia, Y. H. Jin, P. Z. Zhao, C. C. Zhao, M. Q. Jia, L. Wang and X. M. He, *Electrochim. Acta*, 2019, **310**, 230–239.
27 Z. Q. Hao, X. Y. Shi, Z. Yang, L. Li and S. L. Chou, *Adv. Funct. Mater.*, 2022, **32**, 2208093.
28 L. Y. Zhang, P. Xie, X. L. Zhang, B. C. Zhu, T. Liu and J. G. Yu, *J. Colloid Interface Sci.*, 2024, **662**, 1075–1085.
29 X. F. Wang, C. C. Pei, Q. Wang, Y. Hu, H. Wang, H. X. Liu, L. F. Zhang and S. W. Guo, *Inorg. Chem. Front.*, 2022, **9**, 547–558.
30 X. L. Huang, S. Men, H. Zheng, D. D. Qin and X. W. Kang, *Chem.–Asian J.*, 2020, **15**, 1456–1463.
31 Y. A. Huang, M. J. Wang, M. Z. Huang, Y. P. Xiong, X. Yang, Z. R. Miao, Z. Y. Yang and J. Yu, *Electrochim. Acta*, 2022, **414**, 140167.
32 M. Y. Gao, Y. M. Chen, J. Wang, R. Yang, X. M. Guo, F. Cao, S. S. Sun, J. H. Zhang and Q. H. Kong, *Chem. Lett.*, 2022, **51**, 221–223.
33 H. Tian, Z. Z. Xu, K. Liu, D. Wang, L. L. Ren, Y. M. Wei, L. Z. Chen, Y. Y. Chen, S. H. Liu and H. X. Yang, *J. Colloid Interface Sci.*, 2024, **670**, 152–162.
34 T. Yang, M. J. Fang, J. W. Liu, D. X. Yang, Y. H. Liang, J. S. Zhong, Y. J. Yuan, Y. A. Zhang, X. L. Liu, R. K. Zheng, K. Davey, J. Zhang and Z. P. Guo, *Adv. Funct. Mater.*, 2022, **32**, 2205880.
35 F. Huang, L. Wang, D. C. Qin, Z. B. Xu, M. Q. Jin, Y. Chen, X. X. Zeng and Z. H. Dai, *ACS Appl. Mater. Interfaces*, 2022, **14**, 1222–1232.
36 H. Zheng, D. K. Ma, M. J. Pei, C. K. Lin, Y. Liu, S. Q. Deng, R. X. Qiu, Y. Y. Luo, W. Yan and J. J. Zhang, *Adv. Funct. Mater.*, 2025, **35**, 2411651.
37 T. Liu, Y. Yang, S. W. Cao, R. H. Xiang, L. Y. Zhang and J. G. Yu, *Adv. Mater.*, 2023, **35**, 2207752.
38 W. N. Li, X. P. Lu, B. W. Biney, J. F. Li, Y. C. Yan and K. Chen, *J. Colloid Interface Sci.*, 2025, **677**, 312–322.
39 X. Zhang, R. Duan, T. J. Zheng, P. T. Chen, X. W. Yu, Z. J. Qiao and D. B. Ruan, *Chem. Eng. J.*, 2024, **498**, 155232.
40 H. Zheng, D. K. Ma, M. J. Pei, C. K. Lin, Y. Liu, S. Deng, R. X. Qiu, Y. Y. Luo, W. Yan and J. J. Zhang, *Adv. Funct. Mater.*, 2025, **35**, 2411651.
41 X. W. Li, J. Y. Sun, W. X. Zhao, Y. J. Lai, X. Yu and Y. Liu, *Adv. Funct. Mater.*, 2022, **32**, 2106980.